Granular Matter (2023) 25:3
https://doi.org/10.1007/s10035-022-01290-y

ORIGINAL PAPER

Systematic design of particle dampers for transient vertical vibrations

Niklas Meyer[1] · **Robert Seifried**[1]

Received: 13 May 2022 / Accepted: 21 October 2022

Abstract
A multilevel design toolchain is used for the development of particle dampers for vertical transient vibrating structures. Thereby various experimental tests and numerical models are combined. The design toolchain consists of three levels. The first level deals with the micro-mechanical behavior of single particle–particle and particle–wall impacts. The resulting coefficient of restitution is then used on the second level. Within, the second level the properties of vertical vibrated granular matters inside a container under harmonic motion are analyzed. The resulting motion modes and energy dissipation of the granular matter strongly depend on the excitation conditions, i. e. the excitation amplitude and excitation frequency. Multiple analytical formulations for the different motion modes, i. e. solid-like state and collect-and-collide motion mode, are derived to describe the energy dissipation within the particle damper. These analytical descriptions are in good agreement with numerical discrete element simulations. Finally, the third level of the design toolchain deals with designing a damper for a desired structure. The analytical formulations describing the energy dissipation within the particle damper are used to optimize a particle damper configuration for a simple beam-like structure undergoing a vertical transient vibration. The efficiency of the optimized particle damper dissipation is proven experimentally.

Keywords Particle damper · Design toolchain · Vertical vibrations · Granular material · DEM · Complex power

1 Introduction

Particle dampers (PD) are a useful tool to reduce undesired vibrations of technical applications in various fields. For that, particles are filled in containers attached to the vibrating structure or placed in cavities within the structure itself. By structural vibrations, momentum is transferred to the particles and the granular matter starts interacting with each other. Friction and inelastic collisions between the particles lead to an energy dissipation inside the damper, reducing the structural vibration.

In 1937 Paget [24] developed the very first particle damper using a single particle, nowadays referred to as an impact damper. As a derivative of these classical impact dampers, particle dampers use many particles and show the same robust properties against harsh environmental conditions [25, 36]. In many cases, they add only little mass to the system [14] and can be applied to a wide frequency range [4, 33].

The big drawback of particle dampers is their highly nonlinear behavior and multitude of influence parameters, which are rarely understood in detail. This currently hinders the wide industrial application of particle dampers. Thus, in [18] a systematic multiscale design methodology in form of a three-step *toolchain* is developed to support the damper design and damper integration into a structure, see Fig. 1. Here, the nonlinear processes within the particle damper are analyzed on different scales or levels, respectively. This starts with micro-mechanical effects during single particle impacts and sliding contacts, continues with the energy dissipation inside the particle container subjected to a defined vibration and concludes with the interaction within a structure. Insights made on one level can be used on the next level to improve the understanding of the dynamical properties and reduce the overall design process of particle dampers. This design toolchain is based on computational models as well as models derived from experiments. Thus, these

This article is part of topical collection: Energy transport and dissipation in granular systems.

✉ Robert Seifried
robert.seifried@tuhh.de
http://www.tuhh.de/mum

[1] Institute of Mechanics and Ocean Engineering, Hamburg University of Technology, Eißendorfer Straße 42, 21073 Hamburg, Germany

Published online: 02 December 2022

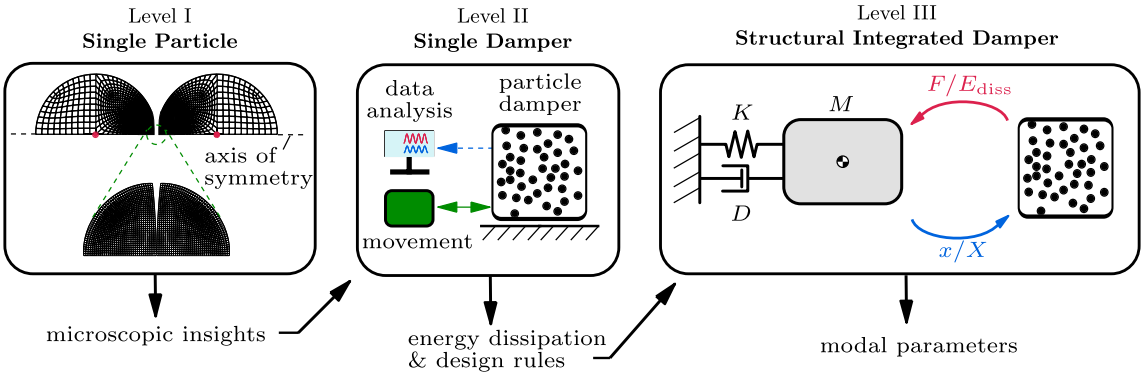

Fig. 1 Toolchain for the analysis of particle dampers

models provide very useful insights into the complex processes, nonlinear effects and design parameters influencing the efficiency of particle dampers.

In this paper, the design toolchain is applied for the development of a particle damper to attenuate the free vertical vibration of a simple beam-like structure setup. The system exhibits a low first eigenfrequency and only small material damping is present. While for the horizontal vibrating case, the system has been excessively studied, see [18, 21], in the vertical case, the particle damper exhibits completely different particle motions, which have not been described in full detail yet.

On Level I of the design toolchain, the coefficients of restitution of single particle–particle and particle–wall interactions are analyzed. This provides important input for the simulations carried out on the next level.

On Level II, *motion modes* (of the rheological behavior), also referred to as state of matter, *energy dissipation* and *effective particle mass* in vertically driven particle dampers are analyzed for a given excitation amplitude range and excitation frequency range using the *discrete element method* (DEM). The energy dissipation of the occurring particle normal contacts is hereby controlled by the coefficients of restitution determined on the first level of the toolchain. The obtained DEM results are henceforth referred to as *effective fields*. From these results, design rules and analytical formulas describing the energy dissipation in the damper are derived. These analytical formulas are computationally very efficient and allow then for a fast dimensioning process of particle dampers on Level III.

Related studies on motion modes have been conducted in [2, 7, 29, 40, 41], on the energy dissipation in [6, 16, 17, 38, 40, 41] and on analytical formulations in [3, 16]. Though, different excitation frequencies and excitation amplitudes are often analyzed. Thus, so far no comprehensive design guideline exists for low frequency vertical vibrations as described here.

On Level III of the toolchain, the particle damper is integrated numerically and experimentally into a simple beam-like structure setup to obtain its overall damping effect. Numerically, the simple beam-like structure is described by a reduced finite element model. First, different models of the particle damper, i. e. a DEM model, the effective fields and analytical formulations obtained on the second level of the toolchain, are coupled to the simple beam-like structure model. A good agreement between experiments and all utilized models is achieved for an initial deflection of the system and the following free vibration. Finally, the model based on the analytical formulations is used for a damper optimization for the previously used initial deflection. The efficiency of the optimized damper design is proven experimentally.

It should be noted that the used toolchain has already been presented in detail and applied to low frequency horizontal vibrations in [18]. Hence, the presentation follows [18]. However, the presented results here are completely new and unique, as the dynamical behavior of the particle damper is different for horizontal and vertical vibrations. This is because completely different motion modes are observed for these two vibration directions. For horizontal vibrations, particles first roll over the container base, fluidize, and finally enter a bouncing state for increasing excitation intensity. For vertical vibrations, however, multiple different bouncing states are observed, e. g. if particles reach the top container side or not. A comprehensive description of these bouncing states for vertical vibrations is missing in the literature so far.

This paper is organized in the following way: In the Sects. 2, 3 and 4 the three serial evaluation levels of the toolchain are applied to vertical vibration analysis of low frequencies. In closing, the conclusion is given in Sect. 5.

2 Level I: single particle impacts

The micro-mechanical behavior during the impact of two bodies, i. e. particle–particle or particle–wall, can mainly be characterized by the coefficient of restitution (COR) and the friction coefficient. While the COR describes the energy loss due to the normal impact of two bodies, the friction coefficient models the losses by the tangential relative motion, due to the surface roughness.

Frictional effects are often described by a *static* and *sliding friction coefficient*, i. e. μ_0 and μ, respectively. However, these friction coefficients strongly depend on the surface roughness, adhesion, and lubrication of the colliding bodies and are, hence, difficult to determine [37]. Thus, the friction coefficients can be used as a tuning parameter in the DEM simulations for later particle damper analyses. As the later particle damper is a highly dynamic system it is legitimate to neglect static friction [8]. In [22] it is shown that the usage of a constant friction coefficient is sufficient for accurate DEM simulation results. Thus, the friction coefficient is set to $\mu = 0.1$ for all DEM simulations here, which is a typical value found in literature [12]. However, future studies have to show if a constant friction coefficient also applies to other excitation regimes.

For the determination of the coefficient of restitution ε (COR) for low velocity impacts numerical as well as experimental analyses can be performed [10, 27, 34]. In this paper, the methods and results presented in [23] are used. The impact velocity-dependent COR is obtained from experimental impact tests and numerical finite element simulations, see e. g. Fig. 1 for a schematic representation. For the experimental tests, a steel sphere impacts different fixed planar material probes. The finite element simulations are carried out by an elastic-viscoplastic material model for steel and are in good agreement with the experiments.

The COR for the sphere–wall, i. e. steel–polyvinyl chloride (PVC), and sphere–sphere, i. e. steel–steel, impacts are shown in Fig. 2-*right* and the corresponding material data in Fig. 2-*left* with Young's modulus E, Poisson's ratio ν, and density ρ. A high dependency on impact velocity is observed for sphere–sphere impacts. The COR starts close to one for small impact velocities and drops rapidly when the impact velocity is increased. Finally, the COR converges below 0.5. For the sphere–wall impacts, the COR starts at about 0.9 for small impact velocities. For increasing impact velocities a slight almost linear reduction is observed. At the highest measurable impact velocity of $1.8\,^{\mathrm{m}}/_{\mathrm{s}}$ the COR still has a value of 0.8.

The obtained CORs are used on the second level of the toolchain for DEM simulations to model the energy dissipation during the occurring normal contacts. For this task, the penalty law by Gonthier [11] is used, which is based on Hertz [13] impact theory. Interestingly, during later numerical studies it turns out that the CORs' values are of minor importance for the efficiency of the particle damper for vertical vibrations.

3 Level II: single damper

On this level studies of an isolated particle damper subjected to a vertical vibration are performed, see Fig. 1 for a schematic representation. These investigations can be performed experimentally or numerically, see e. g. [19, 22]. The energy dissipation within the particle damper is obtained for a given excitation frequency range and amplitude range. The amplitude range and frequency range are chosen to match the dynamics of the later employed simple beam-like structure used on Level III, see Sect. 4. As the structure's first eigenfrequency is rather low ($f_0 \approx 5\,\mathrm{Hz}$), a DEM model is utilized for the following investigations. The testbed used in [19, 22] is not suitable for the here required frequency range and amplitude range but has been used to validate the DEM model before. The particle container is excited by a harmonic motion using a rheonomic constraint in vertical direction as $x_c = X \sin(\Omega t)$, with container amplitude X and angular frequency $\Omega = 2\pi f$.

Body	Sphere	Wall
Material	S235	PVC
E [GPa]	208	3
ν [–]	0.3	0.38
ρ [kg/m^3]	7900	1400
μ [–]	0.1 for all contacts	
ε [–]	see Fig. 2-*right*	

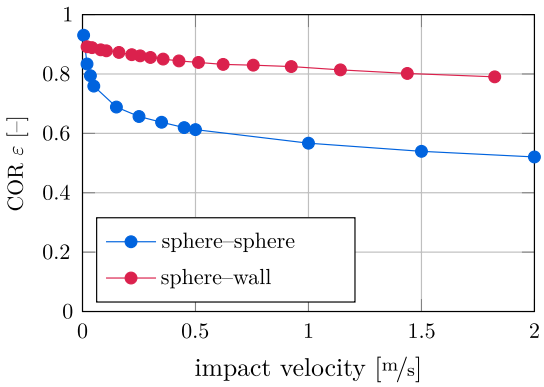

Fig. 2 Material parameters (*left*) and velocity dependent COR (*right*) for the used spheres and walls

The corresponding container velocity and acceleration follow as $\dot{x}_c = V\cos(\Omega t)$ and $\ddot{x}_c = -A\sin(\Omega t)$ with $V = X\,\Omega$ and $A = X\,\Omega^2$.

Discrete element method: The discrete element method (DEM) is a discrete simulation method for granular materials originally invented by Cundall and Strack [5]. Every particle is considered as an unconstrained moving body only influenced by applied forces. The dynamics are described by Newton's and Euler's equation of motion for every particle [26].

In this research, the code presented in [20] is used. For the contact search, the Verlet list in combination with the link cell algorithm is applied. The continuous normal contact forces are calculated using Gonthier's formula [11], which is based on the contact law of Hertz [13] and extended by a nonlinear damping parameter depending mainly on the COR, which controls the amount of energy dissipation during contact. For the tangential forces, sliding friction with friction coefficient μ and an additional smoothing hyperbolic tangent function to avoid jumps in the friction forces at zero velocity [1] is utilized. The time integration is performed using a variable time step fifth order Gear predictor-corrector algorithm [9].

Complex power: To analyze the energy dissipation and the efficiency of particle dampers, the complex power method, introduced by Yang [39], is used. The complex power is determined as

$$P^* = \frac{1}{2}\,F^{*\top}\,\bar{V}^*. \tag{1}$$

In that, F^* denotes the complex amplitude obtained by the fast Fourier transform (FFT) of the driving force signal acting on the container and $\bar{V}^*$ is the conjugate complex amplitude by FFT of the velocity signal of the container motion. For the here performed DEM simulations the velocity of the particle container is given and the driving force is the sum of the container's inertia and the particle contact forces acting in driving direction. The dissipated energy per cycle $\widetilde{E}_{\mathrm{diss}}$ follows from the complex power to

$$\widetilde{E}_{\mathrm{diss}} = 2\,\pi\,E_{\mathrm{diss}} = \frac{2\pi}{\Omega}\cdot \mathrm{Real}(P^*). \tag{2}$$

To judge the damper's efficiency the effective loss factor $\bar{\eta}$ [16, 22] is utilized. It is calculated by a scaling of the dissipated energy with the kinetic energy of the particle system E_{kin} using the mass of the particle bed m_{bed}, i. e. the mass of all particles, to

$$\bar{\eta} = \frac{E_{\mathrm{diss}}}{E_{\mathrm{kin}}} = \frac{E_{\mathrm{diss}}}{\frac{1}{2}\,m_{\mathrm{bed}}\,|V_\Omega^*|^2}, \tag{3}$$

with V_Ω^* being the FFT of the velocity signal at the driving frequency. As a consequence, the effective loss factor is independent of the particle mass and the container mass and enables the comparison of different particle settings.

Another important quantity is the effective moving mass $\bar{M}^*_{\mathrm{mov}}$. It is determined by dividing the complex amplitude of the excitation force signal at driving frequency F^*_Ω by the complex amplitude of the acceleration signal at driving frequency A^*_Ω. By the effective moving mass the *effective particle mass* $\bar{m}_{\mathrm{bed}}$ is obtained. The effective particle mass describes how much mass of the whole particle bed is "felt" by the container, i. e. to what extent the mass of the granular matter is coupled to the container movement [31]. It is achieved to

$$\bar{m}_{\mathrm{bed}} = |\bar{M}^*_{\mathrm{mov}} - m_{\mathrm{con}}| = |\frac{F^*_\Omega}{A^*_\Omega} - m_{\mathrm{con}}|, \tag{4}$$

with m_{con} being the mass of the particle container. When the particle damper is later coupled to an underlying structure, this effective particle mass will cause a decrease in the structure's eigenfrequency. Refer to [18] for detailed information on this topic.

Motion modes: If a particle bed inside a container is subjected to a harmonic vibration, different motion modes (of the rheological behavior) can be observed depending on the granular properties and excitation conditions. To distinguish the different motion modes, animations and velocity fields obtained from DEM simulations as well as experimental observations can be used. This task is not always trivial and unambiguous as the transition between the motion modes is smooth. For vertical vibrations the motion modes have been classified by different authors into solid-like state, local fluidization, global fluidization, undulation, convection, Leidenfrost effect, Buoyancy convection and collect-and-collide state (CaC) [2, 7, 29, 40, 41].

For the single damper analysis here, the same particle container as for the later structural integration is used. The considered particle container is made of PVC. It has a quadratic cross section with an inner edge width of 40mm and a length (L) of 120mm in excitation direction, i. e. in the direction of gravity. Steel particles of 5mm radius are used throughout this paper. In order to obtain a general impression of the motion modes in the low frequency range of the later used simple beam-like structure setup, excitation frequencies between $f = 2\,\mathrm{Hz} - 20\,\mathrm{Hz}$ and excitation strokes between $X = 1\,\mathrm{mm} - 200\,\mathrm{mm}$ are investigated.

The resulting motion modes in the particle damper obtained by DEM simulations are depicted in Fig. 3. Compared to other authors, i. e. [2, 7, 29, 40, 41], significantly lower frequencies are analyzed here as the later utilized structure exhibits a low eigenfrequency. Moreover, fewer particles are used to reduce the numerical effort. As a consequence, only the *solid-like* state and the *collect-and-collide* motion modes are observed. It is expected that this is due

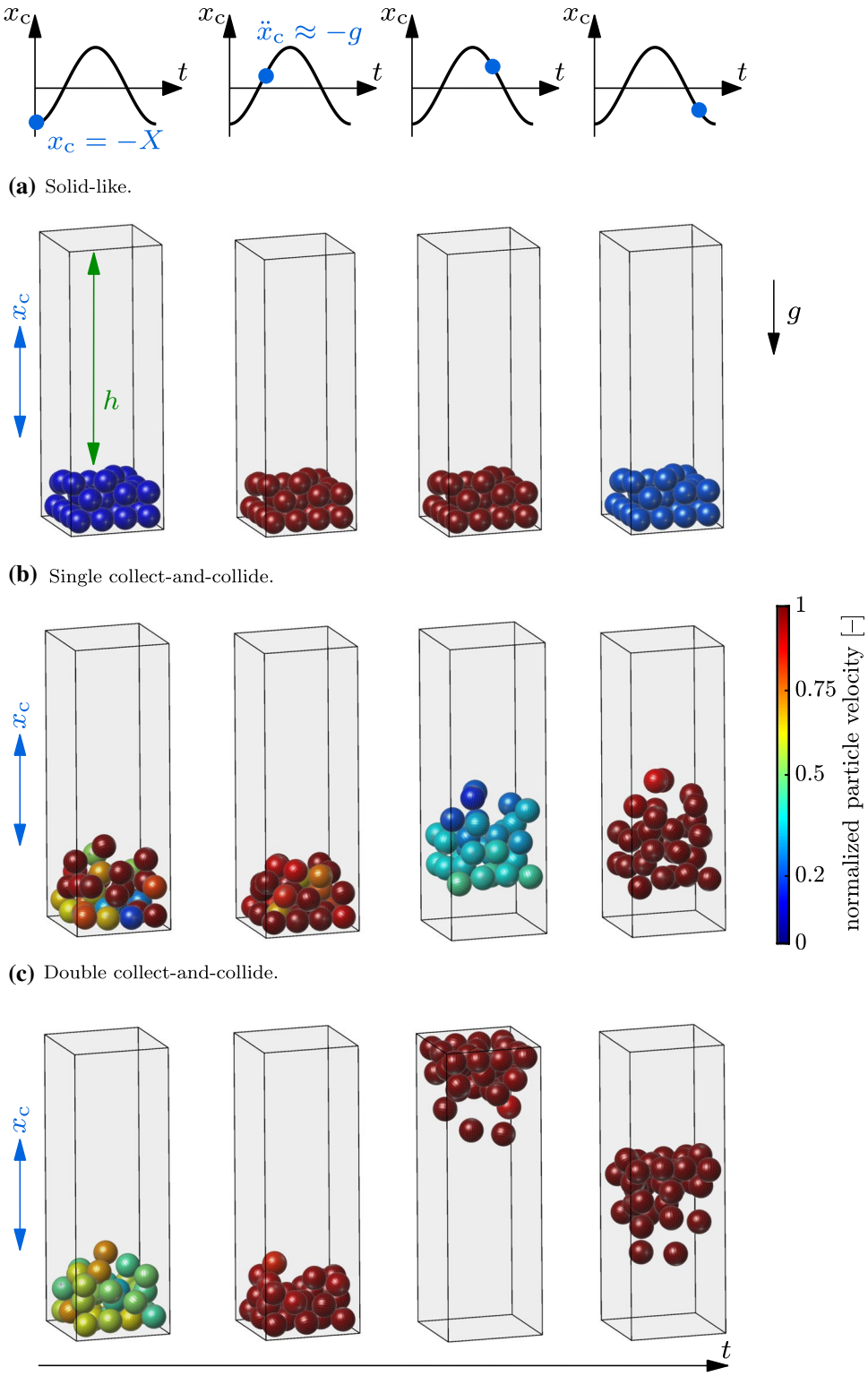

Fig. 3 Observed motion modes at different time steps for one container vibration cycle. The colors show the magnitude of the particle velocity normalized by the container velocity amplitude V from low (*blue*) to high (*red*) (colour figure online)

to the lower frequency and not due to the reduced particle number. However, this needs further investigations.

Within the solid-like state, see Fig. 3a, the particles remain on the container base. Only very little relative motion between the particles is seen. Within the collect-and-collide state, the particles take-off the container base and move up and down as one particle block. This particle block collides inelastically with the container walls, i. e. after impact the particle bed has adopted the container's velocity and does not rebound from it. This happens due to multiple

inter-particle collisions during impact. For further discussions see [3, 32]. Hence, a synchronous particle motion with the container is achieved. This state is further subdivided into *single collect-and-collide* and *double collect-and-collide*. Within the single collect-and-collide state, see Fig. 3b, the particle bed does not reach the upper container wall, but only collides with the container bottom. Within the double collect-and-collide state, see Fig. 3c, the particle bed reaches the upper container wall. Hence, a collision with the lower and upper container walls is achieved. Under certain conditions, as will be discussed later, a scattered motion mode is observed, where the particle system begins to scatter and no regular motion is seen anymore. As this motion mode evolves from the collect-and-collide motion modes and exhibits no representative movement, it is not shown in Fig. 3.

3.1 Analytical descriptions

In the following, analytical descriptions of the particle bed's motion modes and energy dissipation shall be derived for vertical vibrations under gravity. Afterward, the analytical results are compared and validated via DEM analyses. Furthermore, some design parameters are analyzed using the DEM model. The derived analytical descriptions are numerically much more efficient than the DEM simulations and can later be used for designing a damper for an underlying structure. Some experimental results will be given later in Sect. 4.

3.1.1 Derivation of analytical formulations

In order to set up the analytical equations for the energy dissipation of the particle bed, some assumptions on the particle motion have to be made. These are based on insights of the DEM simulations and can also be observed from the motion modes seen in Fig. 3. As detected in Fig. 3 the particle bed stays together and moves as one particle block for the considered motion modes. This means that the translational velocities of the particles are the same. The particle rotations are only of minor magnitude for the considered frequency and amplitude range and are thus neglected for the analytical descriptions, see e. g. [3]. Initially, the particle bed is located at the container's bottom. When the container moves upwards, the particle bed will take-off the container bottom if $\ddot{x}_c \leq -g$ holds with g being the gravitational constant. The particle bed collides in the following either with the lower or upper container wall. This depends on the excitation conditions and the clearance h, i. e. the distance from the particle bed to the upper container wall, see also Fig. 3. When the particle bed collides with either container wall, an inelastic collision occurs, i. e. the particle bed instantaneously adopts the velocity of the container wall. The inelastic nature of the collision is justified in [3, 32] and occurs due to multiple inter particle–particle and particle–wall impacts. Even though only a small amount of energy is dissipated in every single collision, an inelastic collision is achieved due to the accumulated energy dissipation.

Using the assumptions stated in the previous paragraph different trajectories of the particle bed are obtained as displayed in Fig. 4. The trajectories are shown until the first impact of the particle bed with the container bottom occurs. If a trajectory ends at the upper container wall, it implies that this trajectory does not lead to a repetitive particle motion. Instead, the scattering motion mode is seen in DEM simulations.

In Fig. 4 the same motion modes as in Fig. 3 are visible, i. e. solid-like state, single collect-and-collide and double collect-and-collide. However, these motion modes can be further subdivided into:

1. *Solid-Like State* (e. g. $X = 15\,\text{mm}$ and $f = 4\,\text{Hz}$)
2. *Single Collect-and-Collide*
   - (i) Harmonic impact with container bottom (e. g. $X = 15\,\text{mm}$ and $f = 6\,\text{Hz}$)
   - (ii) Subharmonic impact with container bottom (e. g. $X = 15\,\text{mm}$ and $f = 10\,\text{Hz}$)
3. *Double Collect-and-Collide*
   - (i) Harmonic impact with container top and bottom (e. g. $X = 50\,\text{mm}$ and $f = 18\,\text{Hz}$)
   - (ii) Harmonic impact with container top and subharmonic impact with container bottom (conditionally repetitive particle trajectory) (e. g. $X = 20\,\text{mm}$ and $f = 18\,\text{Hz}$)
   - (iii) Subharmonic impact with container top (no repetitive particle trajectory) (e. g. $X = 15\,\text{mm}$ and $f = 14\,\text{Hz}$)

First of all, the motion mode of the particle bed has to be determined for the different excitation conditions. The particle bed is in the solid-like state as long as the container acceleration amplitude is below the gravitational constant, i. e. $A < g$. For higher container accelerations the particle bed will take-off the container bottom. Then, the system is either in the single collect-and-collide or double collect-and-collide motion mode. The time when the particle bed takes-off the container bottom $t_{\text{off}}^{\text{bot}}$, also referred to as *take-off time*, is obtained by numerically solving the take-off condition

$$A \sin\left(\Omega\, t_{\text{off}}^{\text{bot}}\right) = g, \tag{5}$$

with the condition $0 < \Omega\, t_{\text{off}}^{\text{bot}} < \frac{1}{2}\pi$. Next, it has to be determined whether the particle bed impacts the container top

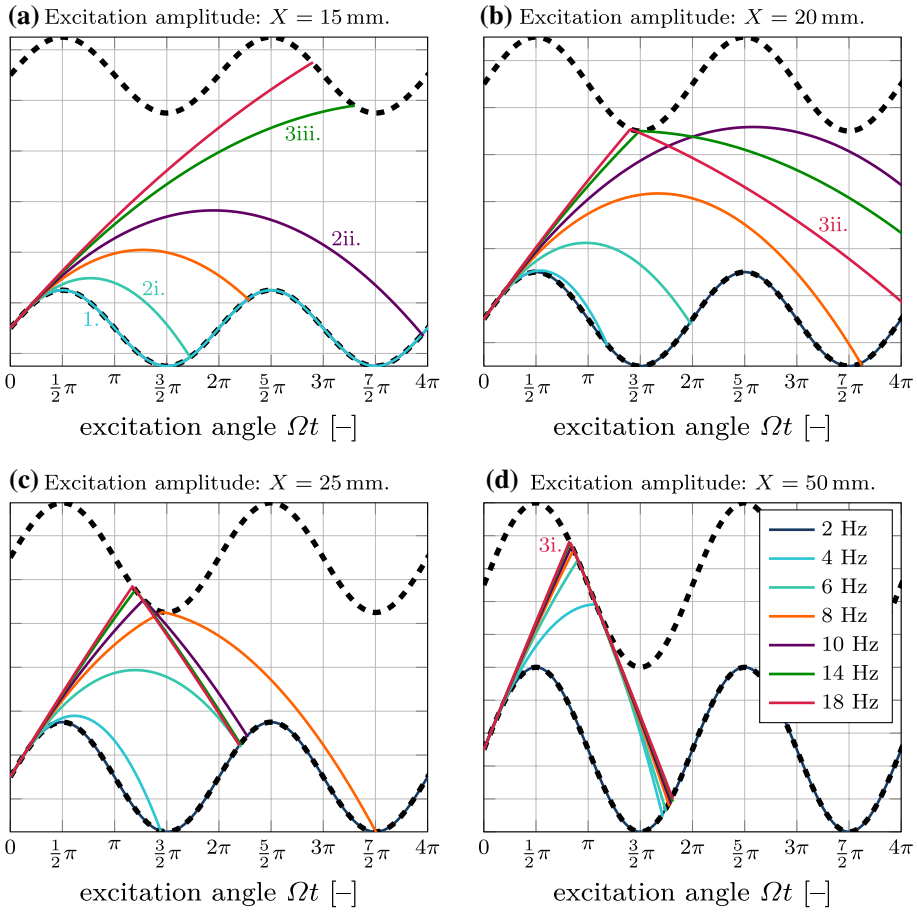

Fig. 4 Trajectories of particle bed for vertical vibrations for different excitation frequencies and amplitudes with $h = 0.1$ m. The black dashed line indicates the motion of the top and bottom container walls

or not. If so, the double collect-and-collide motion mode is achieved. Otherwise, the single collect-and-collide motion mode is obtained. After the particle bed takes-off the container bottom, a parabolic flight occurs. Using the particle bed's take-off position $x_{\mathrm{off}}^{\mathrm{bot}} = x_{\mathrm{c}}(t_{\mathrm{off}}^{\mathrm{bot}})$ and the particle bed's take-off velocity $\dot{x}_{\mathrm{off}}^{\mathrm{bot}} = \dot{x}_{\mathrm{c}}(t_{\mathrm{off}}^{\mathrm{bot}})$ an impact with the container top occurs if a solution to the following impact condition exists

$$x_{\mathrm{off}}^{\mathrm{bot}} + \int_{t_{\mathrm{off}}^{\mathrm{bot}}}^{t_{\mathrm{imp}}^{\mathrm{st}}} \left(\dot{x}_{\mathrm{off}}^{\mathrm{bot}} - g\ (t - t_{\mathrm{off}}^{\mathrm{bot}})\right)\mathrm{d}t \quad = X \sin(\Omega\, t_{\mathrm{imp}}^{\mathrm{st}}) + h, \tag{6}$$

$$\Rightarrow \underbrace{x_{\mathrm{off}}^{\mathrm{bot}} + \dot{x}_{\mathrm{off}}^{\mathrm{bot}}\, \Delta t_{\mathrm{st}} - \frac{1}{2}\, g\, \Delta t_{\mathrm{st}}^2}_{\text{particle motion}} \quad = \underbrace{X \sin(\Omega\, t_{\mathrm{imp}}^{\mathrm{st}})}_{\text{container motion}} + \underbrace{h}_{\text{clearance}}. \tag{7}$$

The impact time point with the upper container wall is denoted by $t_{\mathrm{imp}}^{\mathrm{st}}$, i. e. the first impact of the particle bed, and $\Delta t_{\mathrm{st}} = t_{\mathrm{imp}}^{\mathrm{st}} - t_{\mathrm{off}}^{\mathrm{bot}}$ is the flight duration of the particle bed. The clearance between the particle bed and the upper container wall h is shown in Fig. 3 and can be calculated by $h = L\left(1 - \frac{n_{\mathrm{p}}}{n_{\mathrm{p}}^{\mathrm{max}}}\right)$ with $n_{\mathrm{p}}^{\mathrm{max}}$ being the maximum possible particle number to fit in the container and n_{p} being the actual particle number in the container.

Now it is possible to distinguish between the different motion modes using Eqs.(5) and (7). In the next step, the dissipated energy for every motion mode will be derived.

3.1.1.1 Solid-like state In the solid-like state the particles do not take-off the container bottom. As a result, only very little relative motion between the particles occurs. An accurate analytical description is therefore not possible. The dissipated energy per cycle is approximated by comparisons to DEM results to 0.1 % of the particles' kinetic energy as

$$\widetilde{E}_{\mathrm{diss}} = \frac{2\,\pi}{1000}\, E_{\mathrm{kin}} = \frac{\pi}{1000}\, m_{\mathrm{bed}}\, V^2. \tag{8}$$

3.1.1.2 Single collect-and-collide The particle system is in the single collect-and-collide state if a solution to Eq. (5) exists but not to Eq. (7), i. e. the particle bed takes-off the container bottom but does not collide with the container top.

Instead, the particle bed collides with the container bottom again. The impact time point with the container bottom $t^{\mathrm{st}}_{\mathrm{imp}}$ is obtained by solving

$$\underbrace{x^{\mathrm{bot}}_{\mathrm{off}} + \dot{x}^{\mathrm{bot}}_{\mathrm{off}}\,\Delta t_{\mathrm{st}} - \frac{1}{2}\,g\,\Delta t^2_{\mathrm{st}}}_{\text{particle motion}} = \underbrace{X\sin(\Omega\, t^{\mathrm{st}}_{\mathrm{imp}})}_{\text{container motion}}. \tag{9}$$

Note, except for the clearance, Eq. (9) is identical to Eq. (7).

For a harmonic impact with the container bottom this motion mode results in one inelastic collision per vibration cycle. Thus, the dissipated energy per cycle follows to

$$\widetilde{E}_{\mathrm{diss}} = \kappa\,\frac{1}{2}\,m_{\mathrm{bed}}\,\Delta v^2_{\mathrm{st}}, \tag{10}$$

$$\Delta v_{\mathrm{st}} = \underbrace{\dot{x}^{\mathrm{bot}}_{\mathrm{off}} - g\,\Delta t_{\mathrm{st}}}_{\text{particle velocity}} - \underbrace{\dot{x}^{\mathrm{st}}_{\mathrm{imp}}}_{\substack{\text{container}\\ \text{velocity}}}, \tag{11}$$

with Δv_{st} being the relative velocity between particle bed and container at impact. The velocity of the container at the time of impact is $\dot{x}^{\mathrm{st}}_{\mathrm{imp}} = \dot{x}_{\mathrm{c}}(t^{\mathrm{st}}_{\mathrm{imp}})$. The variable κ is a scaling of the dissipated energy for subharmonic particle impacts with the container bottom, see e. g. Fig. 4-2ii. In contrast to horizontal vibrations [15], these subharmonic impacts lead to repetitive particle trajectories. This is observed by the utilized DEM simulations. The variable κ follows to $\kappa = 1/(1+n_{\mathrm{s}})$, with $n_{\mathrm{s}} \in \mathbb{N}_0$ being the number of the vibration cycle at particle impact with the container bottom. The number of the vibration cycle at particle impact n_{s} follows from the impact time point as

$$\frac{5}{2}\,\pi + 2\,\pi\;(n_{\mathrm{s}}-1) < \Omega\, t^{\mathrm{st}}_{\mathrm{imp}} < \frac{5}{2}\,\pi + 2\,\pi\, n_{\mathrm{s}}, \tag{12}$$

see also Fig. 4. It is noted that a vibration cycle is considered from $\frac{1}{2}\pi$ till $\frac{5}{2}\pi$. Their exist a small range for the impact time point for which the particle's take-off condition is violated, i. e. for $2\pi + \Omega\, t^{\mathrm{bot}}_{\mathrm{off}} < \Omega\, t^{\mathrm{st}}_{\mathrm{imp}} < \frac{5}{2}\pi$. This means that the particle bed impacts the container bottom when the container's acceleration is already below g, i. e. the time point when the particle bed normally takes-off. Here, however, it is observed from DEM simulations that a repetitive particle trajectory is still achieved. By impact, the particles rebound from the container base, which is hard to analytically describe. Still, Eq. (10) can be used as a rough approximation for the energy dissipation as will be shown later.

3.1.1.3 Double collect-and-collide The double collect-and-collide motion mode occurs if a solution to Eqs. (5) and (7) exists, i. e. an impact with the container top. The particle bed will "take-off" the container top when the container acceleration raises above $-g$. This time point can be expressed by using the take-off time from the container bottom, i. e. the solution to Eq. (5). If the collision with the container top occurs at a container acceleration above $-g$, the particle bed directly rebounds from the container top. The take-off time from the container top $t^{\mathrm{top}}_{\mathrm{off}}$ is thus achieved to

$$t^{\mathrm{top}}_{\mathrm{off}} = \max\left(\underbrace{t^{\mathrm{st}}_{\mathrm{imp}}}_{\text{rebound}},\ \underbrace{\frac{\pi}{\Omega} - t^{\mathrm{bot}}_{\mathrm{off}}}_{\ddot{x}_{\mathrm{c}}=-g}\right). \tag{13}$$

In this equation a subharmonic impact with the container top is not considered, see e. g. Fig. 4-3iii. This is due to the fact that DEM simulations have shown that these do not lead to a repetitive particle trajectory, i. e. a scattering of the particle system occurs instead. In these cases, Eq. (8) is used to approximate the energy dissipation of the particle bed.

After the particle bed takes-off the container top, a parabolic flight until impact with the container bottom occurs. Defining the take-off position from the container's top $x^{\mathrm{top}}_{\mathrm{off}} = x_{\mathrm{c}}(t^{\mathrm{top}}_{\mathrm{off}})$ and the take-off velocity from the container's top $\dot{x}^{\mathrm{top}}_{\mathrm{off}} = \dot{x}_{\mathrm{c}}(t^{\mathrm{top}}_{\mathrm{off}})$, the time of impact $t^{\mathrm{nd}}_{\mathrm{imp}}$ with the container bottom, i. e. the second particle impact, follows by solving

$$\underbrace{x^{\mathrm{top}}_{\mathrm{off}} + \dot{x}^{\mathrm{top}}_{\mathrm{off}}\,\Delta t_{\mathrm{nd}} - \frac{1}{2}\,g\,\Delta t^2_{\mathrm{nd}}}_{\text{particle motion}} = \underbrace{X\sin(\Omega\, t^{\mathrm{nd}}_{\mathrm{imp}})}_{\text{container motion}} - \underbrace{h}_{\text{clearance}}, \tag{14}$$

with $\Delta t_{\mathrm{nd}} = t^{\mathrm{nd}}_{\mathrm{imp}} - t^{\mathrm{top}}_{\mathrm{off}}$ being the flight duration of the particle bed from the container's top to bottom.

Consequently, for the double collect-and-collide motion mode, two impacts of the particle bed with the container walls (top and bottom) occur during one vibration cycle. Hence, the dissipated energy per cycle follows for this motion mode to

$$\widetilde{E}_{\mathrm{diss}} = \kappa\,\frac{1}{2}\,m_{\mathrm{bed}}\left(\Delta v^2_{\mathrm{st}} + \Delta v^2_{\mathrm{nd}}\right), \tag{15}$$

$$\Delta v_{\mathrm{st}} = \dot{x}^{\mathrm{bot}}_{\mathrm{off}} - g\,\Delta t_{\mathrm{st}} - \dot{x}^{\mathrm{st}}_{\mathrm{imp}}, \tag{16}$$

$$\Delta v_{\mathrm{nd}} = \underbrace{\dot{x}^{\mathrm{top}}_{\mathrm{off}} - g\,\Delta t_{\mathrm{nd}}}_{\text{particle velocity}} - \underbrace{\dot{x}^{\mathrm{nd}}_{\mathrm{imp}}}_{\substack{\text{container}\\ \text{velocity}}}, \tag{17}$$

with Δv_{st} and Δv_{nd} being the relative velocities of the particle bed and container at impact with the container's top and bottom, respectively. The variable $\dot{x}^{\mathrm{nd}}_{\mathrm{imp}} = \dot{x}_{\mathrm{c}}(t^{\mathrm{nd}}_{\mathrm{imp}})$ denotes the

velocity of the container at the time of impact with the container bottom. The variable κ is again a scaling for subharmonic impacts onto the container bottom and is defined analogously as for the single collect-and-collide motion mode, i. e. $\kappa = 1/(1 + n_s)$ with n_s being the number of the vibration cycle at particle impact. Here, the latter follows to

$$\frac{5}{2}\pi + 2\pi\ (n_s - 1) < \Omega\, t_{imp}^{nd} < \Omega\, t_{off}^{bot} + 2\pi\, n_s, \tag{18}$$

see also Fig. 4. This means that for a harmonic impact, i. e. $n_s = 0$, the particle bed has to impact the container bottom before the take-off time of the next vibration cycle. From DEM simulations it is observed that a particle impact after the take-off time of the next vibration cycle but before the container's maximum stroke, i. e. an impact time point of $\Omega\, t_{off}^{bot} + 2\pi\, n_s < \Omega\, t_{imp}^{nd} < \frac{5}{2}\pi + 2\pi\, n_s$, leads to a scattering of the particle bed and no repetitive particle trajectory. In this case, Eq. (8) is applied to approximate the energy dissipation of the particle bed.

For very high container acceleration amplitudes $A \gg g$ the influence of gravity becomes negligible. This is analog to a zero gravity environment. Hence, during one vibration cycle, two identical impacts with the container walls occur. Bannerman et al. [3] and Sack et al. [28] have shown that for zero gravity environments the optimal impact time point of the particle bed with the container wall is at $\Omega\, t_{imp}^{st} = \pi$. At this point, the maximum relative velocity between the particle bed and container is achieved. Furthermore, they derive an analytical equation for the container stroke for this impact time point to

$$X_{opt} = \frac{h}{\pi}. \tag{19}$$

The resulting energy dissipation follows to

$$\widetilde{E}_{diss}^{opt} = 4\, m_{bed}\, V^2. \tag{20}$$

This is the highest possible energy dissipation for the double collect-and-collide motion mode. The maximum achievable effective loss factor $\bar{\eta}_{max}$ of this mode is obtained by inserting Eq. (20) into Eq. (3) to

$$\bar{\eta}_{max} = \frac{4}{\pi} \approx 1.27. \tag{21}$$

As $\bar{\eta}_{max}$ is an efficiency factor, it is used later to judge the efficiency of the different motion modes and damper designs.

3.1.2 Validation

In the next step, the derived analytical equations for the energy dissipation of the particle bed shall be validated. This is done by comparing the results of the analytical equations to DEM simulations. The same particle container and excitation conditions as introduced at the beginning of Sect. 3 are used for this task. This particle container is also integrated into a structure in Sect. 4. Using the DEM model, 14 excitation frequencies and 24 excitation amplitudes are analyzed. Every configuration is simulated for a duration of eight vibration cycles, whereas the first two cycles are cut off to remove the irregular particle movement introduced through the initial conditions. In Fig. 5 the results of the analytical equations and DEM simulation for the setting of 32 steel particles of 5mm radius are compared.

In Fig. 5a the predicted motion modes obtained by the analytical equations are shown, i. e. by Eqs. (5) and (7). The transitions between the different motion modes can also be observed by the particle bed's trajectories in Fig. 4. For container acceleration amplitudes of $A < g$ the solid-like state is seen. When the container acceleration amplitude reaches g, the single collect-and-collide–harmonic impact motion modes occurs. From this state, transitions in different motion modes are possible, depending on the container's stroke amplitude X, excitation frequency f and clearance h. However, the influence of the clearance shall not be discussed further in this paper.

For excitation frequencies up to $f = 6\,\text{Hz}$ the system directly exhibits the double collect-and-collide–harmonic impact motion mode. For higher excitation frequencies, the system first of all changes into the single collect-and-collide–subharmonic impact motion mode. From this state transitions into the scattering motion mode or double collect-and-collide–subharmonic impact motion mode are seen. Especially, at high excitation frequencies $f > 12\,\text{Hz}$, the motion modes are very sensitive to the container stroke amplitude and change quickly. In any case, the system reaches the double collect-and-collide–harmonic impact motion mode when the container stroke amplitude gets high enough, i. e. such that $A \gg g \wedge X > X_{opt}$.

In Fig. 5b the effective loss factor obtained from DEM simulations is shown, i. e. the dissipated energy of the particle bed scaled by its kinetic energy, see Eq. (3). A yellow color indicates an effective loss factor of one or higher. A dark blue color indicates an effective loss factor of 0.1 or less. For the solid-like state, only very low values are achieved. This is reasonable, as there is only very little relative motion between the particles in this state. By crossing over to the single collect-and-collide–harmonic impact motion mode much higher effective loss factors up to $\bar{\eta} = 0.7$ are reached. Turning into the single collect-and-collide–subharmonic impact, double collect-and-collide–subharmonic impact or scattering motion mode, a strong reduction within the effective loss factor is observed with values of $0.1 < \bar{\eta} < 0.3$. In the last motion mode, the double collect-and-collide–harmonic impact, a very wide range of effective loss factor values is seen with $0.25 < \bar{\eta} < 1.25$.

(a) Motion modes obtained from analytical equations.

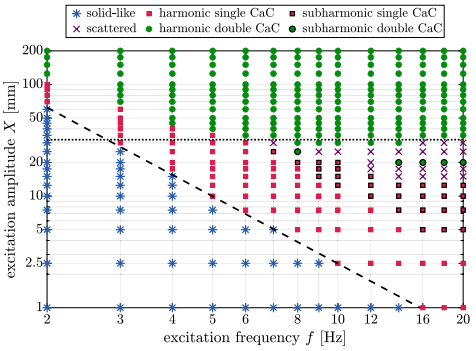

(b) Effective loss factor obtained by DEM simulations.

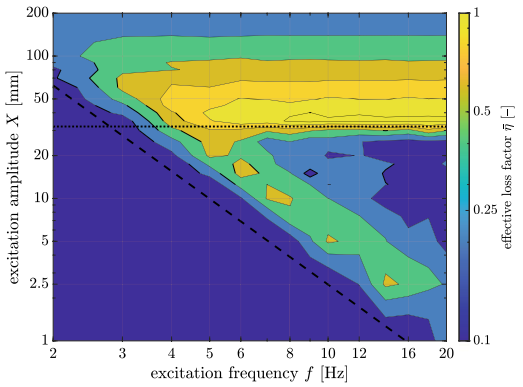

(c) Effective loss factor obtained by analytical equations.

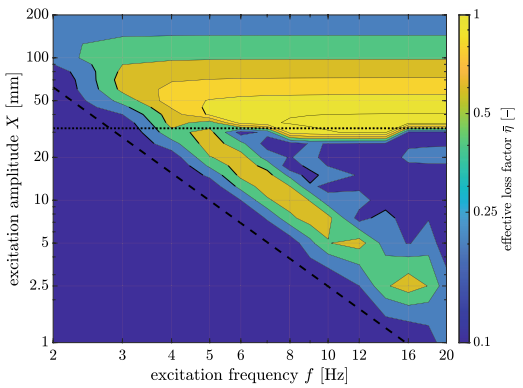

(d) Ratio of effective particle mass to the mass of particle bed obtained from DEM simulations.

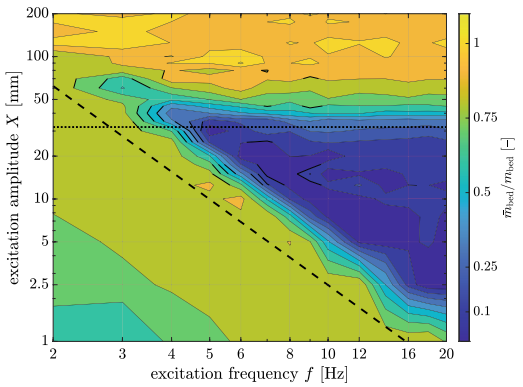

Fig. 5 Results of 32 steel particles of 5mm radius inside rectangular particle container. The black dashed line indicates a constant container acceleration amplitude of $A = g$. The black dotted line indicates a container stroke amplitude of $X_{\mathrm{opt}} = 32\,\mathrm{mm}$. CaC: collect-and-collide

Using Eq. (19) the optimal stroke is calculated for the utilized system to $X_{\mathrm{opt}} = 32\,\mathrm{mm}$. This value is depicted in Fig. 5b as a dashed line and is in good agreement with the high effective loss factor values. In the DEM simulations, the optimal stroke occurs at slightly higher values. This is probably due to the influence of gravity as the optimal stroke is derived for the assumption of a zero gravity environment, see [3]. The maximum obtained effective loss factor by DEM simulations of $\bar{\eta} = 1.25$ is very close to the theoretical optimal one of $\bar{\eta}_{\mathrm{max}} = 1.27$, see Eq. (21). Only for excitation frequencies $f < 5\,\mathrm{Hz}$, i. e. when the container acceleration amplitude A becomes close to g, the effective loss factor is rapidly decreasing at this optimal stroke.

Another important property of the double collect-and-collide–harmonic impact motion mode can be observed starting from the optimal stroke. A high gradient in the effective loss factor is seen for lower container strokes. Here, the system quickly turns into the single collect-and-collide or scattering motion mode. For higher container strokes as the optimal one, only a small gradient in the effective loss factor is observed. Here, the system is still in the double collect-and-collide–harmonic impact motion mode, but the relative impact velocity between particles and container is smaller. For further explanations see [18, 28].

In Fig. 5c the effective loss factor obtained from the analytical equations is depicted. For all motion modes, a good approximation of the effective loss factor to the DEM simulations is achieved. Especially in the single collect-and-collide–harmonic impact and double collect-and-collide–harmonic impact, the values are in good agreement. However, little local areas of higher discrepancies occur for the other motion modes, i. e. the subharmonic and scattering motion modes. This is not surprising as the transition between these modes is sharp and little differences between the DEM model and analytical equations can lead to an entirely different particle motion. This leads to a different energy dissipation and consequently to a different effective loss factor. These differences, among others, are the size of the clearance or a not completely inelastic collision between the particle bed and container wall.

For the scattering motion mode no accurate analytical description exists either and the dissipated energy and thus the effective loss factor are merely approximated. This is can not be seen in Fig. 5, as DEM and analytical formulas lead both to effective loss factors below 0.1, i. e. to a dark blue color. Hence, this difference is of minor importance for a later damper design.

In Fig. 5d the ratio of effective particle mass to the mass of the particle bed obtained by DEM simulations is shown, see Eq. (4). The effective particle mass $\bar{m}_{\mathrm{bed}}$ described to what extent the particle bed mass is coupled to the container motion. For the solid-like and double collect-and-collide–harmonic impact motion modes rather high ratios of $0.5\,m_{\mathrm{bed}} < \bar{m}_{\mathrm{bed}}$ are achieved. This implies that the effective loss factor and effective particle mass are not coupled to each other as for these two motion modes completely different effective loss factors are obtained, see Fig. 5b. For the single collect-and-collide–harmonic impact motion mode medium effective mass ratios of about $0.5\,m_{\mathrm{bed}} < \bar{m}_{\mathrm{bed}} < 0.75\,m_{\mathrm{bed}}$ are obtained. For the other motion modes, i. e. scattering and subharmonic impact, low ratios are seen $\bar{m}_{\mathrm{bed}} < 0.5\,m_{\mathrm{bed}}$.

It seems like a shorter contact time with the container results in a lower effective mass. However, an analytical description of the effective particle mass is hard to derive. For Level III of the toolchain, i. e. the structural integration of the particle damper, the effective particle mass will be approximated as follows:

$$\bar{m}_{\mathrm{bed}} = \begin{cases} 0.75\,m_{\mathrm{bed}} & \text{for solid-like,} \\ 0.75\,m_{\mathrm{bed}} & \text{for harmonic double collect-and-collide,} \\ 0.65\,m_{\mathrm{bed}} & \text{for harmonic single collect-and-collide,} \\ 0.2\,m_{\mathrm{bed}} & \text{for subharmonic double collect-and-collide,} \\ 0.2\,m_{\mathrm{bed}} & \text{for subharmonic single collect-and-collide,} \\ 0.1\,m_{\mathrm{bed}} & \text{for scattering.} \end{cases} \tag{22}$$

3.2 Design parameters

By analyzing the DEM simulations and the analytical formulas, some design parameters can be identified. From the analytical formulas, a linear dependency of the energy dissipation on the particles' bed mass is obtained and thus a linear dependency on the particles' density. Moreover, only a low influence of the other material properties like Young's modulus or particle radius is obtained, due to the inelastic collision behavior of the particle bed. Sanchez [30] shows that the harmonic double collect-and-collide motion mode is unaffected by the particle shape and fragmentation as these properties have no influence on the inelastic collision behavior. Hence, this is also assumed for the other motion modes here. However, this requires further investigations.

For container acceleration amplitudes below the gravitational constant, the presented damper design is not suited to provide sufficient energy dissipation rates, due to the small amount of relative motion between the particles. For higher container acceleration amplitudes as the gravitational constant, an operation in the harmonic double collect-and-collide motion mode should be targeted. Especially at the optimal stroke, very high effective loss factor values and thus energy dissipation rates are obtained. Using the clearance h between the particle bed and the opposite container wall, the optimal stroke can be designed in a targeted manner. For container acceleration amplitudes only slightly above the gravitational constant, the influence of gravity is still

dominant and the system operates in the harmonic single collect-and-collide motion mode. Medium to high effective loss factor values are still achieved, providing sufficient damping. The scattered and subharmonic motion modes should be avoided as only low effective loss factor values can be reached.

4 Level III: structural integrated damper

The last level of the toolchain, see Fig. 1, represents the integration of the particle damper into a vibrating structure. Thus, the overall damping of the system can be determined. The utilized system here is a *simple beam-like structure* setup as shown in Fig. 6. It consist of a 680 mm long elastic beam with rectangular profile of 80 mm × 6 mm and an Young's modulus of $E = 200\,\text{GPa}$. The beam has a fixed support on one side. On the other side, the particle damper including an additional mass is mounted with a total weight of 1270 g. The inner dimensions of the cuboid PVC particle damper are 120 mm × 40 mm × 40 mm. This damper has already been analyzed in Sect. 3 for the single damper case of the toolchain. The whole system is deflected using a counterweight of 11kg yielding an initial displacement of $x_0 = -58\,\text{mm}$. As the later-used particle mass is much lower than the counterweight, an additional deflection of the beam due to the particles can be neglected. The system is released by cutting the rope of the counterweight. After release, the position of the end-effector is measured using a laser vibrometer, the *PSV-500* from Polytec, pointing on the top side of the end-effector. The data acquisition is accomplished using the Front-End of the *PSV-500* with a sampling frequency of 250 kHz. As the laser vibrometer measures the end-effector's velocity, it is internally integrated to the position. To remove the initial offset, the initial deflection of the particle damper is added to the measurements.

4.1 Numerical models

To calculate the movement of the simple beam-like structure, different particle damper models can be coupled to a model of the structure. This is discussed extensively in [18] and here only shortly introduced. In the first step, the simple beam-like structure is discretized using the *finite element method* (FEM), see Fig. 6a. The flexible beam is discretized using 100 Timoshenko beam elements. All other components are modeled as rigid bodies and are included as point elements with the corresponding mass. Then, the linear equation of motion is set up. The structural damping is neglected and is added later based on measurements. Using modal reduction the system is reduced in size. Only the first bending vibration mode is considered as it is dominant for the free vibration considered later on. Finally, after rewriting, the equation of motion with end-effector displacement x in bending direction follows to

$$M\ddot{x} + D\dot{x} + Kx = F, \tag{23}$$

with mass $M = 1.139\,\text{kg}$, stiffness $K = 1848\,{}^{\text{N}}/_{\text{m}}$ and measured structural damping, i. e. without

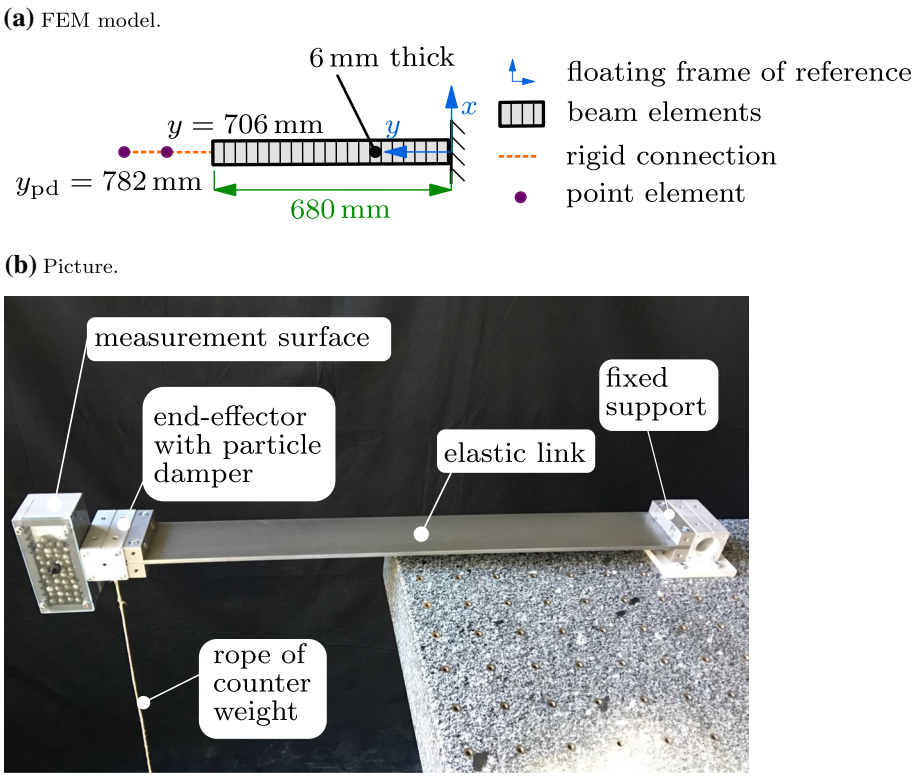

Fig. 6 Composition of the simple beam-like structure setup with FEM model (*top*) and picture (*bottom*)

particles, $D = 0.55\,{}^{\mathrm{kg}}/_{\mathrm{s}}$. The force applied by the particle damper onto the structure is denoted as F. To obtain the particle damper force, different damper models can be used. Here, the three different damper models presented in [18] are used and discussed briefly in the following:

(1) *DEM* The particle damper is modeled by the DEM. Such a model can be seen for instance in Fig. 3. During the simulation, the position of the end-effector x of the simple beam-like structure described by Eq. (23) is applied to the DEM model, i. e. the particle damper itself. Here, the particle accelerations and the reaction forces F onto the container walls are determined. Using the reaction forces, the acceleration $\ddot{x}$ of the end-effector is calculated by Eq. (23). The end-effector's acceleration and the particle states are then integrated in time.

(2) *Effective Fields* The effective fields to describe the particle damper are pre-computed by DEM and shown for instance in Fig. 5. To use the effective fields within Eq. (23), the particle damper force F is replaced by the pseudo forces obtained from the effective fields. The force is replaced as $F = -(\bar{m}_{\mathrm{bed}}\,\ddot{x} + \bar{d}\,\dot{x})$. The effective particle mass $\bar{m}_{\mathrm{bed}}$ follows directly from its corresponding field, see e. g. Fig. 5d. The particle damper's energy dissipation, see e. g. Fig. 5b and Eq. (3), is transformed into an effective viscous damping parameter $\bar{d} = \widetilde{E}_{\mathrm{diss}}/(\pi\,\Omega\,X^2)$, see [35] for details. As the effective particle mass $\bar{m}_{\mathrm{bed}}$ and the effective viscous damping parameter $\bar{d}$ are not constant, they are updated at the minimum position of the particle damper in each vibration cycle. This is justified as all motion modes last for at least one vibration cycle. For the update procedure, the particle damper amplitude X and vibration frequency Ω are necessary, see for instance Fig. 5. The particle damper amplitude X is given at the minimum position of the particle damper, i. e. the end-effector. For the vibration frequency Ω the eigenfrequency of the system is used.

(3) *Analytical Formulas* The coupling of the analytical formulas is performed in the same way as for the effective fields, i. e. the particle damper force is replaced by a pseudo force as $F = -(\bar{m}_{\mathrm{bed}}\,\ddot{x} + \bar{d}\,\dot{x})$. The dissipated energy of the particle damper is obtained from the Eqs. (8),(10) and (15). The effective particle mass is approximated using Eq. (22).

To evaluate and compare the different particle damper models, the damping ratio ζ is used. It follows from the logarithmic decrement as

$$\vartheta = \ln\left(\frac{X_n}{X_{n+1}}\right), \tag{24}$$

$$\zeta = \frac{\vartheta}{\sqrt{4\pi^2 + \vartheta^2}}, \tag{25}$$

with X_n being the vibration amplitude of the n-th vibration cycle. As logarithmic decrement and damping ratio change with the damper amplitude, the mean damper amplitude $X_{n+\frac{1}{2}} = \frac{1}{2}(X_n + X_{n+1})$ is used as sampling point for the damping ratio of the n-th vibration cycle.

4.2 Application to simple beam-like structure

The eigenfrequency of the undamped beam-like structure follows from the numerical model to $f_0 = 5.56\,\mathrm{Hz}$ and fits very well to the experimental measured one of $f_0 = 5.56 \pm 0.02\,\mathrm{Hz}$. By utilizing particles within the damper, the undamped eigenfrequency of the structure will reduce, due to the temporary coupled particle mass. This new eigenfrequency is called *effective eigenfrequency* in the following.

4.2.1 Verification

In the first step, the coupling procedure of the different particle damper models **1**-**3** with the equation of motion of the simple beam-like structure, i. e. Eq. (23), is validated by comparison to a conducted experiment. Therefore, the particle container is filled with 32 steel particles of 5 mm radius weighting 131 g and released from the initial deflection. For DEM simulation, i. e. model **1**, the material data of Fig. 2 are used. The corresponding effective fields, i. e. model **2**, are shown for this setup in Fig. 5. The analytical formulas, i. e. model **3**, are given by Eqs. (8),(10) and (15).

In Figs. 7 and 8 the different trajectories and damping ratios are compared between experiment and simulation utilizing the damper models **1-3**. To give an impression of the additional damping by the particles in Fig. 7 the envelope of the system without particles, i. e. only the structural damping, is shown.

After initial deflection, the particle bed is first in the double collect-and-collide motion mode. The damping ratio in the experiment starts at about $\zeta = 0.035$ for $X = 53\,\mathrm{mm}$ and is increasing while the container amplitude decreases up to $\zeta = 0.05$ at $X = 41\,\mathrm{mm}$. At the next sampling point, the particle bed is already in the single collect-and-collide motion mode. The theoretical value of the optimal stroke for this particle setting, see Eq. (19), is $X_{\mathrm{opt}} = 32\,\mathrm{mm}$ and thus

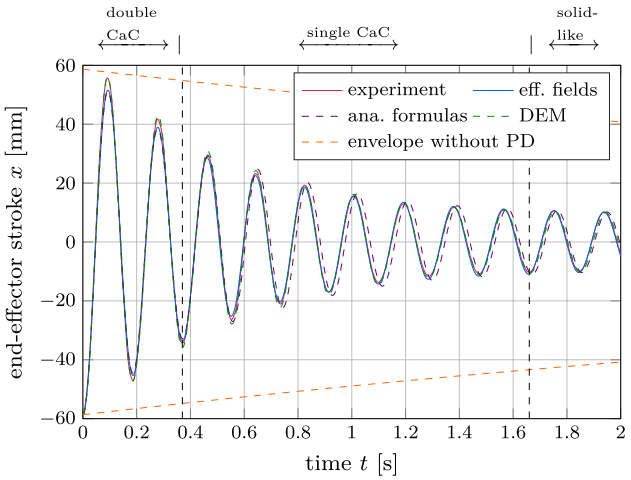

Fig. 7 Comparison of container trajectories between experiment and numerical models **1**-**3** of 32 steel particles of 5 mm radius. The vertical dashed lines indicate the transition from double collect-and-collide to single collect-and-collide to solid-like motion mode obtained by DEM simulation

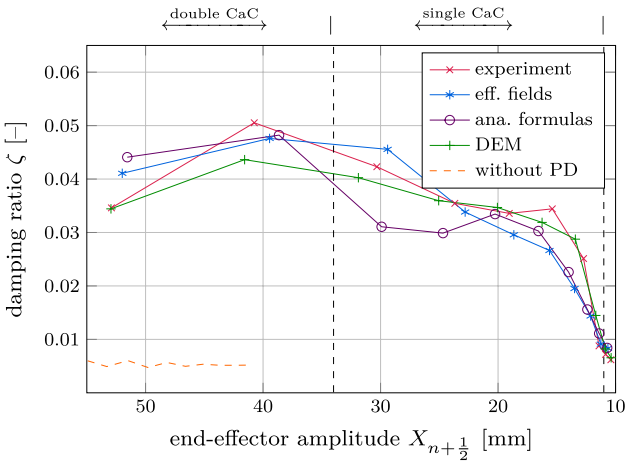

Fig. 8 Resulting damping ratios of Fig. 7

close to the measured high damping ratios and close to the switching point of the particle bed to the single collect-and-collide motion mode, see vertical dashed line in Fig. 8. During the single collect-and-collide motion mode, the damping ratio is decreasing (almost linearly) with decreasing container amplitude. Finally, the particle bed reaches the solid-like state. In this state, hardly any damping by the particles occurs resulting in an almost constant container amplitude.

This nearly constant container amplitude is approximated by the theoretical transition to the solid-like state by $X_{\min} = g/\omega^2 = 8.8\,\text{mm}$ with ω being the eigenfrequency of the system including particles as static mass. From Figs. 7 and 8 it is seen that the end-effector does not reach this minimum amplitude. This happens as the particle bed is already in the solid-like state for slightly higher values than $X_{\min}$. However, compared to the undamped system, a very good damping behavior is achieved. The undamped systems shows damping ratios of about $\zeta = 0.005$ and an amplitude of about $X = 40\,\text{mm}$ after 2 s.

A very good agreement is achieved when comparing the trajectories of the different numerical models to the experiment. The DEM result fits best with the experiment. The trajectories of the effective fields and analytical formulas especially differ from the experimental result at the maximum positive strokes of the end-effector. This happens as the effective viscous damping parameter $\bar{d}$ describing the particle dampers energy dissipation is only updated once per vibration cycle at the negative peaks of the end-effector. Thus, the nonlinear behavior of the particle damper at the impact of the particle bed onto the container walls is not reproduced. However, over one complete vibration cycle the reproduction of the damping behavior is given. For the analytical formulas an additional shift in phase is visible. This phase shift occurs during the single collect-and-collide motion mode and happens because the effective particle mass is only roughly approximated by Eq. (22). As a consequence, the effective eigenfrequency differs between experiment and analytical formulas, resulting in a phase shift.

As the obtained trajectories fit very well, the same is true for the damping ratios. Only for the analytical formulas, two damping values are slightly off, having a negligible effect on the container's trajectory. Although all three numerical models perform very well, their computational costs are very different. The DEM has high online costs, i. e. in the range of hours to days. The analytical formulas and effective fields, however, have very low online costs, i. e. in the range of seconds, but the effective fields have high offline costs. This is because these fields have to be pre-computed by DEM for every new particle setting. Thus, the analytical formulas are computationally most efficient as these can be used for arbitrarily particle numbers.

4.2.2 Optimization

Due to the high numerical efficiency of the analytical formulas, they are used for damper optimization next. The objective is to find the filling ratio of the particle damper to achieve the end-effector's smallest container amplitude after 0.8s. Therefore, the particle number is varied by an increment of 16, i. e. by one layer of particles. Note, the more particles are used, the more energy can theoretically dissipate. However, the higher the used particle number, the smaller the clearance h and thus the smaller the optimal stroke, see Fig. 3 and Eq. (19). A simple brute-force algorithm is used to find the optimal setting. The resulting particle number is 64 weighting 265 g in total. To validate

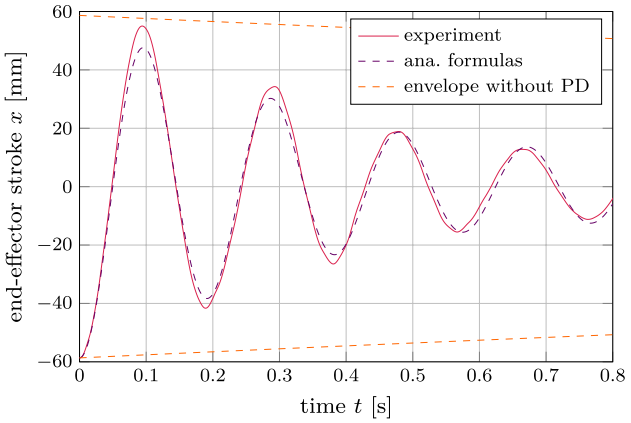

Fig. 9 Comparison of container trajectory for optimized particle number between experiment and analytical result

this optimal analytical result, it is compared to an equivalent conducted experiment as shown in Fig. 9.

In the experiment, great damping is achieved. After 0.75 s the system's end-effector has almost reached its minimum stroke $X_{\min} = 10\,\text{mm}$. At this time point, the system's end-effector shown in Fig. 7 is at 19 mm amplitude. The simulation by the analytical formulas is in good agreement with the experiment. Especially, the negative peaks of the end-effector match by amplitude. The phase difference between the experiment and the analytical result is small. Hence, a good damping setting is found using this simple optimization procedure.

5 Conclusion

To enable a systematic design of particle dampers, a multilevel design toolchain is used in this work. The toolchain is applied to analyze and design particle dampers for low frequency vertical vibrations. For this task, the design toolchain is separated into three serial levels. Level I analyzes the microscopic behavior of single particle–particle and particle–wall impacts. The resulting coefficient of restitution shows a high dependency on impact velocity and is used on the next level for DEM simulations.

On Level II, a particle damper is subjected to a vertical vibration using a rheonomic constraint. Thus, the particle damper can be analyzed without an underlying structure, which gives important insights into its nonlinear behavior. Multiple motion modes are observed within the DEM simulations, namely, the solid-like, single collect-and-collide, double collect-and-collide and scattering motion modes. For the solid-like state, the particle bed remains on the container base, resulting in only very little energy dissipation rates. Within the single collect-and-collide motion mode the particle bed takes-off the container's base but does not reach its top. Hence, only medium energy dissipation rates are obtained. Instead, for the double collect-and-collide motion mode, the particle bed impacts the container top, resulting in possible high energy dissipation rates. The scattering state occurs for specific conditions and should be avoided due to low energy dissipation rates. The derived analytical equations describing the energy dissipation for all motion modes are in good agreement with numerical DEM simulations. These formulations are independent of the specific particle damper and can be used to efficiently design particle dampers to damp vertical vibrating structures.

Finally, on Level III of the toolchain, the particle damper is applied to damp a simple beam-like structure. The different numerical models of the particle damper are coupled to a modal reduced model of the structure. A good agreement between simulations and experiment is observed. Lastly, a damper optimization is performed using the analytical equations and later validated experimentally. Hence, the development of particle dampers for vertical vibrations becomes sophisticated in a straightforward way with no need for exhausting trial and error experiments.

Acknowledgements The authors would like to thank the German Research Foundation (DFG) for the financial support of the project 424825162. The authors would also like to thank Dr.-Ing. Marc-André Pick, Dipl.-Ing. Riza Demir, Dipl.-Ing. Norbert Borngräber-Sander and Wolfgang Brennecke for helping to design and realize the experimental rig.

Funding Open Access funding enabled and organized by Projekt DEAL.

Declarations

Conflict of interest On behalf of all authors, the corresponding author states that there is no conflict of interest.

References

1. Andersson, S., Söderberg, A., Björklund, S.: Friction models for sliding dry, boundary and mixed lubricated contacts. Tribol. Int. **40**(4), 580–587 (2007). https://doi.org/10.1016/j.triboint.2005.11.014

2. Ansari, I.H., Alam, M.: Patterns and velocity field in vertically vibrated granular materials. AIP Conf. Proc. **1542**(1), 775–778 (2013). https://doi.org/10.1063/1.4812046
3. Bannerman, M.N., Kollmer, J.E., Sack, A., Heckel, M., Mueller, P., Pöschel, T.: Movers and shakers: granular damping in microgravity. Phys. Rev. E (2011). https://doi.org/10.1103/PhysRevE.84.011301
4. Chen, T., Mao, K., Huang, X., Wang, M.: Dissipation mechanisms of nonobstructive particle damping using discrete element method. Proc. SPIE - The Int. Soc. Opt. Eng. **4331**, 294–301 (2001). https://doi.org/10.1117/12.432713
5. Cundall, P.A., Strack, O.D.L.: A discrete numerical model for granular assemblies. Int. J. Rock Mech. Min. Sci. Geomech. **16**(4), 47–65 (1979). https://doi.org/10.1680/geot.1979.29.1.47
6. Duan, Y., Chen, Q.: Simulation and experimental investigation on dissipative properties of particle dampers. J. Vib. Control. **17**(5), 777–788 (2010). https://doi.org/10.1177/1077546309356183
7. Eshuis, P., Weele, K., Meer, D., Lohse, D.: Granular leidenfrost effect: experiment and theory of floating particle clusters. Phys. Rev. Lett. **95**, 258001 (2006). https://doi.org/10.1103/PhysRevLett.95.258001
8. Fleissner, F., Gaugele, T., Eberhard, P.: Applications of the discrete element method in mechanical engineering. Multibody Sys. Dyn. **18**(1), 81–94 (2007). https://doi.org/10.1007/s11044-007-9066-2
9. Gear, C.W.: The numerical integration of ordinary differential equations of various orders. Math. Comput. **21**(98), 146 (1967). https://doi.org/10.2307/2004155
10. Goldsmith, W.: Impact: the theory and physical behavior of colliding solids. Edward Arnold Publishers, London (1960). https://doi.org/10.1115/1.3641808
11. Gonthier, Y., McPhee, J., Lange, C., Piedbœuf, J.C.: A regularized contact model with asymmetric damping and dwell-time dependent friction. Multibody Sys.Dyn. **11**(3), 209–233 (2004). https://doi.org/10.1023/B:MUBO.0000029392.21648.bc
12. He, H., Senetakis, K., Coop, M.R.: An investigation of the effect of shearing velocity on the inter-particle behavior of granular and composite materials with a new micromechanical dynamic testing apparatus. Tribol. Int. **134**, 252–263 (2019). https://doi.org/10.1016/j.triboint.2019.02.002
13. Hertz, H.: Über die Berührung fester elastischer Körper (On the contact of stiff elastic solids). J. für die Reine Angew. Math. **92**, 156–171 (1882). https://doi.org/10.1515/crll.1882.92.156
14. Johnson, C.D.: Design of passive damping systems. J. Mech. Des. **117**(B), 171–176 (1995). https://doi.org/10.1115/1.2838659
15. Kollmer, J.: Probing the validity of an effective-one-particle description of granular dampers in microgravity. Granul. Matter (2014). https://doi.org/10.1007/s10035-014-0539-8
16. Masmoudi, M., Job, S., Abbes, M.S., Tawfiq, I., Haddar, M.: Experimental and numerical investigations of dissipation mechanisms in particle dampers. Granul. Matter **18**(3), 71 (2016). https://doi.org/10.1007/s10035-016-0667-4
17. Matchett, A.J., Yanagida, T., Okudaira, Y., Kobayashi, S.: Vibrating powder beds: a comparison of experimental and distinct element method simulated data. Powder Technol. **107**(1), 13–30 (2000). https://doi.org/10.1016/S0032-5910(99)00080-7
18. Meyer, N., Schwartz, C., Morlock, M., Seifried, R.: Systematic design of particle dampers for horizontal vibrations with application to a lightweight manipulator. J. Sound Vib. **510**, 116319 (2021). https://doi.org/10.1016/j.jsv.2021.116319
19. Meyer, N., Seifried, R.: Experimental and numerical investigations on parameters influencing energy dissipation in particle dampers. VI International Conference on Particle-based Methods - Fundamentals and Applications pp. 260–271 (2019)
20. Meyer, N., Seifried, R.: Numerical and experimental investigations in the damping behavior of particle dampers attached to a vibrating structure. Comput. Struct. **238**, 106281 (2020). https://doi.org/10.1016/j.compstruc.2020.106281
21. Meyer, N., Seifried, R.: Optimal design of particle dampers for structures with low first eigenfrequency under forced vibration. 7th edition of the International Conference on Particle-based Methods (2021). https://doi.org/10.23967/particles.2021.022
22. Meyer, N., Seifried, R.: Toward a design methodology for particle dampers by analyzing their energy dissipation. Comput. Part. Mech. **8**(4), 681–699 (2021). https://doi.org/10.1007/s40571-020-00363-0
23. Meyer, N., Wagemann, E.L., Jackstadt, A., Seifried, R.: Material and particle size sensitivity analysis on coefficient of restitution in low-velocity normal impacts. Comput. Part. Mech. (2022). https://doi.org/10.1007/s40571-022-00471-z
24. Paget, A.L.: Vibration in steam turbine buckets and damping by impacts. Engineering **143**, 305–307 (1937)
25. Panossian, H.: Non-obstructive particle damping experience and capabilities. Proc. SPIE - The Int. Soc. Opt. Eng. **4753**, 936–941 (2002). https://doi.org/10.2514/6.2008-2102
26. Pöschel, T.: Computational Granular Dynamics: Models and Algorithms. Springer, Berlin (2005). https://doi.org/10.1007/3-540-27720-X
27. Pöschel, T., Brilliantov, N.V.: Extremal collision sequences of particles on a line: optimal transmission of kinetic energy. Phys. Rev. E **63**(2), 1–9 (2001). https://doi.org/10.1103/PhysRevE.63.021505
28. Sack, A., Heckel, M., Kollmer, J., Zimber, F., Pöschel, T.: Energy dissipation in driven granular matter in the absence of gravity. Phys. Rev. Lett. (2013). https://doi.org/10.1103/PhysRevLett.111.018001
29. Saluena, C., Esipov, S.E., Poeschel, T., Simonian, S.S.: Dissipative properties of granular ensembles. Proceedings of SPIE Volume 3327, Smart Structures and Materials 1998: passive damping and isolation pp. 23–29 (1998). https://doi.org/10.1117/12.310696
30. Sanchez, M., Carlevaro, C.M., Pugnaloni, L.: Effect of particle shape and fragmentation on the response of particle dampers. J. Vib. Control **20**(12), 1846–1854 (2014). https://doi.org/10.1177/1077546313480544
31. Sanchez, M., Pugnaloni, L.: Effective mass overshoot in single degree of freedom mechanical systems with a particle damper. J. Sound Vib. (2011). https://doi.org/10.1016/j.jsv.2011.07.016
32. Sanchez, M., Rosenthal, G., Pugnaloni, L.: Universal response of optimal granular damping devices. J. Sound Vib. **331**(20), 4389–4394 (2012). https://doi.org/10.1016/j.jsv.2012.05.001
33. Schönle, A., Gnanasambandham, C., Eberhard, P.: Broadband damping properties of particle dampers mounted to dynamic structures. Exp. Mech. (2022). https://doi.org/10.1007/s11340-022-00882-2
34. Seifried, R., Minamoto, H., Eberhard, P.: Viscoplastic effects occurring in impacts of aluminum and steel bodies and their influence on the coefficient of restitution. J. Appl. Mech. (2010). https://doi.org/10.1115/1.4000912
35. Shabana, A.A.: Theory of Vibration: An Introduction, 3 edn. Springer, New York (2019). https://doi.org/10.1007/978-1-4612-3976-5
36. Simonian, S.S.: Particle beam damper. Proceedings of SPIE Volume 2445, Smart Structures and Materials 1995: Passive Damping pp. 149–160 (1995). https://doi.org/10.1117/12.208884
37. Urbakh, M., Klafter, J., Gourdon, D., Israelachvili, J.: The nonlinear nature of friction. Nature **430**, 525–528 (2004). https://doi.org/10.1038/nature02750
38. Wong, C.X., Daniel, M.C., Rongong, J.A.: Energy dissipation prediction of particle dampers. J. Sound Vib. **319**(1–2), 91–118 (2009). https://doi.org/10.1016/j.jsv.2008.06.027

39. Yang, M.Y., Lesieutre, G.A., Hambric, S., Koopmann, G.: Development of a design curve for particle impact dampers. Noise Control Eng. J. **53**, 5–13 (2005). https://doi.org/10.1117/12.540019
40. Yin, Z., Su, F., Zhang, H.: Investigation of the energy dissipation of different rheology behaviors in a non-obstructive particle damper. Powder Technol. (2017). https://doi.org/10.1016/j.powtec.2017.07.090
41. Zhang, K., Chen, T., He, L.: Damping behaviors of granular particles in a vertically vibrated closed container. Powder Technol. **321**, 173–179 (2017). https://doi.org/10.1016/j.powtec.2017.08.020